Electrodeposited heterostructured manganese oxides on carbonized clothes for enhanced lithium polysulfides conversion as free-standing sulfur cathodes

Journal of Power Sources 580 (2023) 233457

Contents lists available at ScienceDirect

Journal of Power Sources

journal homepage: www.elsevier.com/locate/jpowsour

Electrodeposited heterostructured manganese oxides on carbonized clothes for enhanced lithium polysulfides conversion as free-standing sulfur cathodes

Usman Zubair [a,b,*], Khalil Jori [c], Jorge E. Thomas [d], Julia Amici [a], Carlotta Francia [a], Silvia Bodoardo [a]

[a] Department of Applied Science and Technology, (DISAT), Politecnico di Torino, C.so Duca degli Abruzzi 24, 10129, Torino, Italy
[b] School of Engineering and Technology, National Textile University, Sheikhupura Road, 37610, Faisalabad, Pakistan
[c] INIFTA. Fac. de Cs. Exactas, Universidad Nacional de La Plata - CONICET Diagonal, 113 y Calle 64, 1900, La Plata, Buenos Aires, Argentina
[d] YPF Tecnología S.A., Av. Del Petróleo S/N (e/129 y 143), 1923, Berisso, Buenos Aires, Argentina

HIGHLIGHTS

- MnO_x is electrodeposited on carbonized cellulose cloth from post-consumer waste.
- Different phases of MnO_x are achieved and confirmed through XAS and XPS.
- Interactions of LiPS with MnO_x are underlined using in-situ XAS and XPS.
- High sulfur loading freestanding cathodes with long-life stability are realized.

GRAPHICAL ABSTRACT

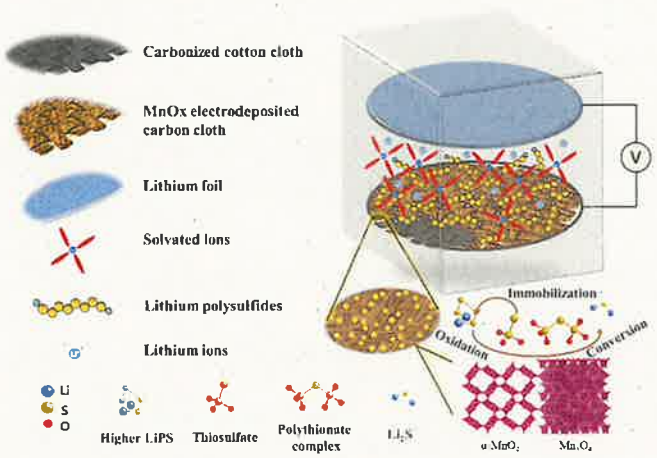

ARTICLE INFO

Keywords:
Li-S battery
Manganese oxide
Polysulfides redox
Surface-bound insoluble intermediates
Surface engineering
Oxygen vacancies

ABSTRACT

Various metal oxides are investigated to catalyse lithium polysulfides (LiPS) conversion to promote the surface-bound insoluble intermediates and limit the LiPS shuttle. Herein, an effective methodology is reported to enhance LiPS catalytic conversion by applying electrodeposited hybrid phase composite films of manganese oxide (MnO_x) on carbonized cotton cloth. Synergistic effects of porous carbon fabric with remnant lumen and high interfacial MnO_x composite film of nanoflakes greatly contribute towards freestanding high-loaded sulfur cathodes. Various MnO_x phases are realized by controlled annealing of MnOOH electrodeposited nanoflakes on carbon cloth. Oxygen deficient phases especially active interfaces among various phases are proposed to accelerate the LiPS oxidation to polythionate complexes that can interact with LiPS to assist their onsite

* Corresponding author. National Textile University, Sheikhupura road, 37610, Faisalabad, Pakistan.
E-mail addresses: usman.zubair@polito.it, usman.zubair@ntu.edu.pk (U. Zubair).

https://doi.org/10.1016/j.jpowsour.2023.233457
Received 25 February 2023; Received in revised form 14 July 2023; Accepted 21 July 2023
Available online 1 August 2023

conversion into sulfides. Pristine and LiPS interacted deposited films are investigated by X-ray photoelectron spectra and X-ray absorption spectra. The cathodes bearing high oxygen-deficient manganese oxide nanoflakes achieve high initial discharge capacity of 1153.7 mA h g^{-1} at 0.1 C and high reversible capacity of 824 mA h g^{-1} at 0.5 C over 200 cycles at sulfur areal loading of 5 mg cm^{-2}, while initial discharge capacity of 1085.9 mA h g^{-1} and reversible capacity of 410 mA h g^{-1} are obtained for MnO_2 rich heterostructure film.

1. Introduction

Lithium sulfur (Li/S) batteries hold the potential to be a system for future generation batteries beyond Li-ion technologies owing to their high theoretical capacity of 1675 Ah Kg^{-1} and energy density of 2600 Wh Kg^{-1} [1]. Additionally, the low price, geological abundance, and environmental benignity of sulfur allow Li/S batteries to appeal scientific community as active material for the next-generation power source. Yet, commercialization of this technology is holdup by several issues including inadequate sulfur utilization, rapid capacity decay, modest volumetric and gravimetric capacities at pack level [2], poor rate performance, anode corrosion and poor Coulombic efficiency [3]. These deficiencies mainly arise from insulating nature of terminal products (i.e., sulfur and Li_2S_2/ Li_2S), volumetric expansion of sulfur, solubility and shuttling of intermediates lithium polysulfides (LiPS), sluggish reaction kinetics [1,3]. The leading glitch is LiPS (Li_2S_x, $4 \leq x \leq 8$) solubility in liquid organic electrolytes and shuttling towards anode that limit the cyclic performance and reaction kinetics [4]. These shortcomings had been extensively addressed in literature from past decade by opting multitude strategies including architecture of cathodes, design of separators, inclusion of interlayers and protection of Li anode surface. Various cathodes' architects have been proposed to solve these problems. Highly porous and conductive matrices have been designed to address the issues of insulation and volume expansion. In this concern, first breakthrough study was carried out using CMK-3 as a conductive porous carbon matrix [5]. Afterwards, meso/micro porous carbons [6], hierarchical porous carbons [7], carbon nanofibers, graphene oxide, graphene [8], and carbon nanotubes have also been investigated. Porous carbon matrices can restrict shuttling of LiPS just by physical confinement, offer conducting pathways and accommodate volumetric expansion towards active component of cathodes. Such materials are also surface functionalized with heteroatoms such as O, N, S, P to afford chemical interactions with LiPS [7,9]. This strategy brought in further improvement in the cycling stability of sulfur cathodes owing to mitigated shuttling phenomena due to chemical interaction of LiPS with cathode's host material. In lieu of heteroatomic doping, conductive polymers such as polyaniline, polypyrrole have also been investigated along with carbonaceous materials to stimulate chemical interactions towards LiPS [10].

Lately, focus has been shifted to nanostructured inorganic polar hosts, so called "sulfiphillic frameworks" because of their augmented chemical interactions with sulfur and LiPS. A series of transition metals inorganic hosts such as metal oxides [11–13], nitrides [14,15], sulfides [10,16], carbides [17], MXenes [18], phosphides [19,20], borides [21], selenides [22], and metal organic frameworks [23] have been considered, which chemically interact with LiPS because of the strong Lewis acid-base interactions. Moreover, several investigations demonstrated that some of these matrices such as Nb_2O_5 [13], VO_xN_y [24], CoS_2 can be viewed as electrocatalysts that simultaneously accelerate the reactions kinetics. This results in realization of high rate and long-life span Li/S batteries. Besides chemisorption and electrocatalysis, a novel mechanism has been put forth that points out the conversion of LiPS to polythionates. Nazar and co-workers reported that δ-MnO_2 nanosheets could in situ yield surface-bound thiosulfate species ($S_2O_3^{2-}$) through redox reaction, and then develop an active polythionate complex ($S_xO_6^{2-}$) which acts as a transfer mediator to limit the LiPS shuttle [25]. They anticipated a "Goldilocks" principle for numerous transition metal oxides that is precisely correlated to their redox potentials. Materials within suitable voltage range ($2.4\ V \leq E_0 \leq 3.05\ V$ versus Li^+/Li) including MnO_2 [26,27], VO_2 and CuO could convert soluble LiPS to insoluble surface-bound polythionate complexes. Metal oxides are relatively facile to synthesize, low cost, and can straightforwardly be scaled up to design host materials for Li/S batteries [4], so they could be materials of choice for sulfur cathodes. It is observed that surface chemistry of metal oxides is decisive towards the catalytic properties [28]. Defects including oxygen vacancies and step edges are the most catalytically active sites on the surfaces of metal oxides that add to catalysis of interacting species [4]. It is an established scientific argument that oxygen vacancies enhance the intrinsic conductivity of transition metal oxides and accelerate the kinetics of surface redox reactions [4,11]. Recent studies have enlightened that the concentration of oxygen vacancies on MnO_2 has remarkable impact on the electrochemical performances of electrodes [29,30]. By rationally inducing the surface oxygen defects, it is expected to improve the activity of MnO_2 [31] and achieve the high-performant Li/S batteries. There are few reports in which this phenomenon has been outwardly outlined [32–34].

Recently, the focus has been shifted to composite cathodes composed of highly porous carbons decorated with transition metal compounds to offer synergistic properties [14,35]. Additionally, the emphasis has been given to achieve higher sulfur content, higher sulfur loading, and low electrolyte to sulfur ratio [3]. Various approaches have been investigated to realize stable sulfur cathodes, but the low sulfur loadings at cathode level limit their practical implementation because of aluminum current collector. Al current collector not only greatly contributes towards inactive mass but also corrodes on recurring redox at electrode that in result materials' pulverization from current collector surface. For this reason, flexible and self-standing carbon cathodes from cotton textiles have been developed to achieve high S loading capability and assure sufficient stability to avoid irreversible capacity losses [36].

Herein, authors came up with the novel idea of electrochemical deposition of MnO_x onto carbonized cellulosic fabric to realize freestanding and high sulfur loaded cathodes. Electrochemical deposition of MnO_2 on different substrates is widely employed strategy to appreciate pseudocapacitive behavior in supercapacitors [37–39]. Surface of metal oxides can be engineered to induce oxygen vacancies to realize different oxidation states via annealing of electrodeposited manganese hydroxide film at different temperature and environment [30,40]. This perspective has been exploited to architect high surface area porous nanoflake films with different oxidation states of Mn onto carbonized cotton fabric to achieve freestanding and high sulfur loading cathodes. In this investigation, cathodes were loaded with 5 mg cm^{-2} of sulfur. Freestanding electrodes enabled not only to get rid of Al current collectors but also reduce the electrode preparation steps. Cotton carbon fabric with remnant lumen cavity and porosity, and high surface area electrodeposited MnO_x film composed of nanoflakes could serve as a model sulfur host by synergistically offering physical confinement and chemical interactions to entrap LiPS at higher loading. The performance of these freestanding cathodes is further improved by inducing oxygen deficient phases through a simple heat treatment under reductive environment. The surface reactivity of the nonstoichiometric MnO_x phases are probed through a combination of X-ray photoelectron spectroscopy (XPS), X-ray adsorption spectroscopy (XAS) and exhaustive electrochemical analysis. From this study, it can be inferred that these uniquely architecture sulfur hosts enable to realize improved electrochemical performance, particularly the one with oxygen deficient phases because of effective interaction of LiPS with host.

2. Experimental section

2.1. Production of carbonized cotton cloth and electrochemical deposition of MnO_x

Cellulose carbon cloth (CCC) was produced by carbonization of postconsumer cotton fabric. For the purpose, cotton cloth was first washed with detergent followed by a rinse with acetone to remove dirt, residual fats, and waxes. Then, cotton cloth was carbonized at 850 °C for 1 h with a heating rate 5 °C min^{-1} under N_2 atmosphere. The carbonization conditions were optimized through a design of experiment at which there is a balance among conductivity and strength of the cellulose carbon cloth. Electrochemical deposition of MnO_x was carried out through anodic chronopotentiometry. The deposition bath was comprised of 0.1 M $Mn(CH_3COO)_2$ and 0.1 M Na_2SO_4. The deposition was performed at a current density of 0.03 mA cm^{-2}. The deposition voltage-time profile can be observed in Fig. S1. The as deposited MnOOH films were dried at 100 °C under ambient atmosphere before annealing under various conditions. To realize different oxidation states of Mn (heterostructure), the as deposited films were subjected to 300 °C, and 400 °C under air and 400 °C under argon environment for 1 h. The sample host for sulfur cathodes were labeled as MnO_x-100 °C/air, MnO_x-300 °C/air, MnO_x-400 °C/air and MnO_x-400 °C/Ar.

2.2. Construction of freestanding high loading sulfur cathodes and cells

For the preparation of freestanding carbon structured sulfur cathodes, 15 mm diameter discs were punched out of MnO_x deposited carbonized cellulosic substrates. Sulfur was dissolved in CS_2, and then the obtained solution was added dropwise on punched cathodes to reach required loading. The impregnated sulfur cathodes were subjected to 80 °C to remove residual moisture and CS_2 on glass slides. It is worth mentioning that CCC and electrodeposited CCC substrates have kept intact their structural stability. For sulfur loaded cathodes, MnO_x/S 300 °C air, MnO_x/S 400 °C air, MnO_x/S 400 °C Ar nomenclature has been adopted. The sulfur loadings were kept at 5 mg cm^{-2} for MnO_x electrodeposited CCC cathodes unless mentioned separately, while the loading for CCC host was maintained at 2.4 mg cm^{-2} owing to limited electrochemical performance. The as-prepared cathodes were assembled against lithium foil with E/S ratio around 7–8 μL mg^{-1} of S.

2.3. Materials characterization

The morphologies of CCC and MnO_x deposited CCC substrates were observed using field-emission scanning electron microscopy (FESEM, JEOL-JSM-6700F). High resolution transmission electron microscopic analyses of MnO_x deposited structures have been carried out using a JEOL JEM-2100 TEM. Elemental mapping of deposit is acquired under TEM by imaging the X-ray signals from composite surface. The XRD patterns were recorded on a Panalytical X'Pert PRO diffractomer with a PIXcel detector, using Cu Kα radiation, under the conditions of 2θ = 10–100° and 2θ step size = 0.03, to observe the crystalline structures of MnO_x deposits. X-ray photoelectron spectroscopy (XPS) analyses of MnO_x deposits and LiPS interacted MnO_x deposits were carried out using a Physical Electronics PHI5800 (USA) multi-technique ESCA system, with a monochromatic Al Kα X-ray radiation. For testing, the samples were placed in an ultrahigh vacuum chamber at 2×10^{-10} Torr. The C1s signal equal to 285 eV was taken as internal calibration. The $MnCO_3$ sample had to be measured using the load compensation source (Flood Gun). The analysis was carried out using the CASA XPS software. The spectra requested for the three samples were measured. The deconvolutions were carried out and the species were identified and quantified in a relative manner according to the literature. According to the information of the Mn3s spectra, an average oxidation state was estimated for each of the samples according to the literature. All X-ray Absorption Near Edge Structure (XANES) measurements at the Mn K edge were performed at the DXAS beamline of LNLS, Campinas, Brazil. Equipped with a curved Si 111 crystal as monochromator that achieve an energy resolution of around 0.7 eV. The obtained absorption spectra were treated by standard methods using Athena software.

2.4. LiPS adsorption assessment and Li_2S nucleation test

For LiPS adsorption visual assessment test, the solid Li_2S_6 was prepared by reacting S_8 and Li_2S with molar ratio of 5:1. Firstly, the solution was prepared in an appropriate amount of tetrahydrofuran (THF) by mixing and heating at 50 °C under vigorous magnetic stirring for 48 h and, then solvent was evaporated. The 15 mg solid Li_2S_6 was dissolved in 30 ml DME: DIOX mixture with 1/1 vol ratio. Then, the solution is divided into six parts; one is kept as a control, and in the others 1 cm^2 swatches of CCC, MnO_x-300 °C/air, MnO_x-400 °C/air and MnO_x-400 °C/Ar deposited CCC electrodes have been introduced. The mixture was stirred and observed for visual color change after 6 h. For Li_2S nucleation and growth test, likewise prepared solid Li_2S_8 was dissolved in tetraglyme (TGDME, Sigma) to obtain 200 mM solution. The CCC, MnO_x-300 °C/air, MnO_x-400 °C/air and MnO_x-400 °C/Ar deposited CCC electrodes were soaked with 20 μL Li_2S_8/tetraglyme solution and used as 12 mm electrodes for test. H2010 separator and Li were saturated with 20 μL 1 M LiTFSI/tetraglyme solution and used for coin cell assembling. Li_2S nucleation and growth tests were performed by first galvanostatically discharging the cell to 2.06 V at 0.112 mA and then potentiostatically discharging under 2.05 V until the current was below 10^{-5} A.

2.5. Electrochemical measurements

The coin cells 2032 were assembled using CCC/S, MnO_x/S 300 °C air, MnO_x/S 400 °C air, MnO_x/S 400 °C Ar cathodes versus metallic lithium anode with H2010 (trilayer PP/PE/PP, Celgard) separator with electrolyte to sulfur (E/S) ratio 6–7 μL mg^{-1} of sulfur. Coin cells 2032 were assembled in Ar-filled dry glove box (Mbraun Labstar with O_2 and H_2O < 0.1 ppm). The geometric area of the electrodes was 1.76 cm^2. A lithium disc (16 × 0.2 mm, Chemetall s.r.l.) was employed as an anode. The H2010 separator 20 mm × 20 μm was soaked with the electrolyte composed of 1,2-dimethoxyethane (DME) and 1,3-dioxolane (DIOX) 1:1 (v/v) with 1 M lithium bis(trifluoromethanesulfonyl)imide (CF_3SO_2N-$LiSO_2CF_3$, LiTFSI) and 0.25 M lithium nitrate ($LiNO_3$). Cells were galvanostatically discharged to 1.8 V and charged to 2.6 V vs. Li/Li^+ by an Arbin BT-2000 battery tester at room temperature. Cycling tests were performed at various C-rates. For long-term cycling, as prepared cells were galvanostatically charged and discharged (GCD) between 1.8 and 2.6 V at 0.01 C for the 1st cycle and then onward cycling was performed at 0.2 C. The C-rate was calculated using the theoretical capacity of sulfur (i.e.) 1672 mA′h g^{-1}. Cyclic voltammetry (CV) and electrochemical impedance spectroscopy (EIS) measurements were carried out by CH instrument electrochemical workstation using three electrodes configuration with Li/Li^+ as reference and counter electrodes. CV of MnOx-300 °C/air, MnOx-400 °C/air and MnOx-400 °C/Ar deposited CCC electrodes were carried out between 1.7 and 3.7 V at 0.01 mV s^{-1}, while CV of MnO_x/S 300 °C air, MnO_x/S 400 °C air, MnO_x/S 400 °C Ar cathodes were performed vs. Li between 1.5 and 3.3 V. The wide potential ranges were used to verify the stability of host matrices and to underline the possible redox reactions that can happen in provided electrochemical systems [25]. Electrochemical impedance spectra (EIS) were measured from 1 Hz to 100 kHz with a potential amplitude of 10 mV for MnO_x deposited electrodes and MnO_x deposited sulfur cathode at open circuit potential, after one CV and after 5 CV cycles.

2.6. Post-mortem XPS, EDX and XANES analysis of disassembled cells

The exhausted coin cells were disassembled in Ar glove box and transferred for analyses under inert atmosphere to avoid contamination and air interaction. Energy dispersive X-ray spectroscopy (EDS) of the

separators recovered from exhausted cells were performed using JEOL-JSM-6700F. Elemental mapping is acquired under FESEM by imaging the X-ray signals from separators' surface. XPS of exhausted MnO_x sulfur cathodes were performed to observe the change in heterostructure and oxidation states of Mn in real time working electrodes. For the same purpose, XANES analyses of exhausted MnO_x sulfur cathodes were also performed.

3. Results and discussion

3.1. Freestanding electrochemical MnO_x deposited porous carbon electrode fabrication

The carbon materials from waste biomaterials such as cotton, dry fruits shell have been extensively investigated for their applications in field of energy because of their low cost, ease of processing, sustainability, substantial porosity, and excellent thermal conductivities [36, 41,42]. In current research, a simple approach of high temperature carbonization (850 °C under N_2 atmosphere) has been opted for the manufacturing of freestanding carbon electrodes from end-of-life cotton textiles. Carbon from cotton fibers would possess appreciable porosity in addition to remnant lumen that is originating from cellular structure. These carbonized cellulose clothes have been electrodeposited for MnOOH nanoflakes. The process of electrodeposition has been optimized for the targeted morphology. The morphology is in conformity with our understanding of the overpotential at a certain current density during an electrochemical deposition that strongly influences the nucleation. According to Faraday's law, the rate of electrochemical reaction at the electrode is proportional to the extent of electric charge. Hence, the deposition rates can be predicted for different current densities by following relation [37].

$$V = i_k \eta_k E/\rho$$

where 'V' is deposition rate, 'i_k' is current density, 'η_k' is current efficiency, 'E' is the electrochemical equivalent for Mn (0.29282 g $(Ah)^{-1}$) and 'ρ' is the density of Mn (7.21 g cm^{-3}). This relation reveals that the deposition rate has a strong correlation with current density and current efficiency. The MnOOH electrodeposited films have been annealed under various atmosphere at different temperatures to realize different oxidation states of manganese oxides. In order to realize various oxidation states, the annealing temperature and redox environments have been judiciously selected considering previous literature. For example, Mn^{2+} oxidation state can be reached on opting high temperature and highly reductive environment [31]. It is found that beyond 400 °C, MnO_x causes the disintegration of carbon cloth that limits the treatment temperature window. MnO_x deposited carbon cellulose clothes have been infiltrated with elemental sulfur through simple solution diffusion method to realize freestanding sulfur cathodes. The full scheme of the freestanding sulfur cathodes preparation is presented in Fig. 1a. Fig. S1 depicts the voltage-time profile for current electrochemical deposition of MnOOH through anodic chronopotentiometry.

Morphological analyses of as-prepared pristine and electrodeposited carbon fabrics have been initially investigated by FESEM analysis.

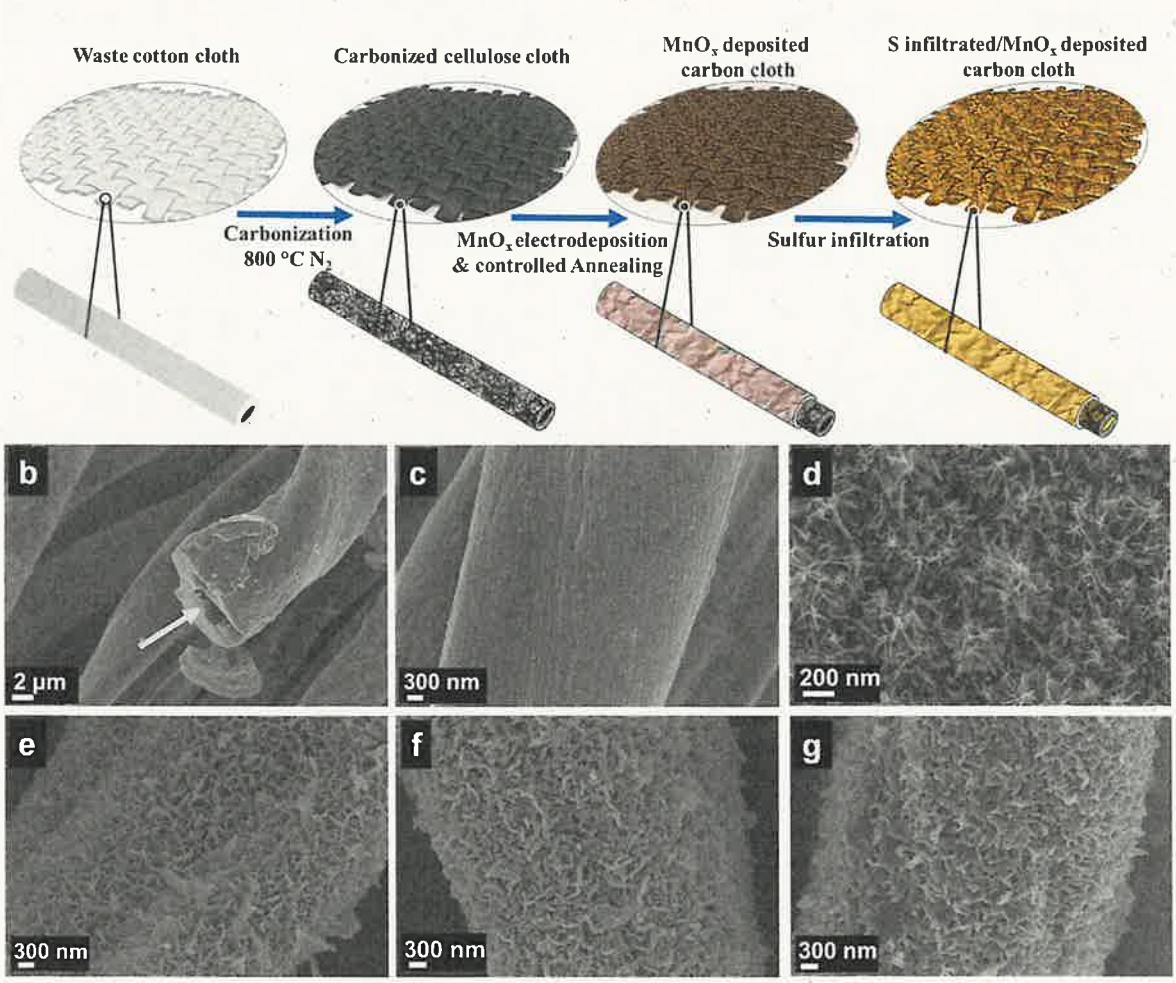

Fig. 1. **(a)** Schematic representation of the procedure opted for the preparation of freestanding MnO_x/S cathodes; FESEM imaging of **(b)** carbonized cotton cloth signifying lumen remnant, **(c)** surface of carbonized fibres, **(d)** non metallized MnO_x 300 °C Air electrodeposited film, chromized electrodeposited films of MnO_x annealed at **(e)** 300 °C Air, **(f)** 400 °C Air, **(g)** 400 °C Ar.

Fig. S2a signifies a 2 × 1 twill weave of carbonized cellulose cloth. While highly corrugated surface of cellulosic carbon fiber with remnant lumen implies the hierarchical porous structure of as-synthesized carbon fibers (Fig. 1b & c).

FESEM of electrodeposited carbon fabric reveals homogenous deposit of MnO_x porous film on carbon fibers as shown in Fig. S2b. On shifting to high resolution, electrochemically deposited MnO_x films has revealed dendritic growth of nanoflakes like that of coral polyp as exhibited in Figs. S2c and 1d. The deposited films are highly porous and uniformly distributed all over the surface of CCC. This distinctive morphology not only imparts the volume to accommodate sulfur and LiPS but also provides a very high surface area to interact with LiPS. After annealing under diverse environment, the porous films maintain similar morphological features with little distortion and agglomeration of nanoflakes. FESEM of annealed samples has been acquired after metal sputtering owing to charging effects that are may be due to loss of intimate contact of MnO_x film and carbon fibers. It can be inferred that the opted route is suitable to transform nanoflakes of manganese oxide into different oxidation states with identical textural properties.

HRTEM analyses of MnO_x deposited films have been performed by recovering them from surface of carbon fabrics. TEM micrograph of MnO_x film annealed at 300 °C exhibited similar nanoflaked morphology but the films annealed at 400 °C cracked into smaller elements during process of samples preparation (Fig. 2). This implies the high surface energy of the deposited film due to strains/defects in the structures owing to oxygen deficient sites. High-angle annular dark field (HAADF) and EDS analyses of MnOOH deposited flakes dried at 100 °C have been performed. In the Fig. S3, amorphous MnOOH nanoflakes with a fragment of carbon fiber from carbonized cellulosic fabrics can be observed. EDS of MnOOH nanoflakes exhibited typical structural elements including Mn, O, and traces of sulfur. This sulfur traces most probably come from sodium sulfate that has been used as electrolyte in electrochemical deposition bath. While the carbon fiber fragment bears the structural elements C and O.

TEM reveals the scale of morphological elements to a few nm that is evidence of high surface to realize effective interaction among MnO_x elements and LiPS. HRTEM depicts the lattice fringes of nanoflakes with interatomic plane spacing of 0.24 nm for MnO_x samples annealed at 300 °C, 0.27 nm for MnO_x sample annealed at 400 °C in air and 0.29 nm for MnO_x sample annealed at 400 °C in argon that particularly correspond to (131) planes of γ-MnO_2, (222) planes of Mn_2O_3, and (112) planes of the tetragonal Hausmannite respectively (Fig. 2b, d, e (insets)). Fig. 2b, d & e (insets) also portray the SAED patterns of as prepared MnO_x samples. This implies the crystalline nature of nanoflakes upon the process of annealing.

XRD analysis has revealed the existence of various phases of MnO_x on diverse heat treatments as exhibited in Fig. 3a. The pattern for MnO_x annealed at 300 °C revealed that the diffraction peaks correspond to the (101), (220), (102) and (222) planes, implying the existence of γ-MnO_2 as per JCPDS # 14–0644 [43,44]. However, it can be observed that diffraction peaks are broad and low that indicate the relatively lower degree of crystallization. XRD diffraction pattern for MnO_x annealed at 400 °C in air has shown the peaks that can be traced back to α-MnO_2 (JCPDS No. 44–0141) and Mn_2O_3 (JCPDS No. 41–1442) diffraction planes [45,46]. While XRD pattern for MnO_x annealed at 400 °C in argon has exhibited diffraction peaks that corresponds to Mn_3O_4 as per JCPDS # 18–0803 [47]. Rietveld refinement of spectra of MnO_x annealed at 400 °C in air and Ar revealed that crystal lattices of these phases belong to space groups I 4/m and I 41/a m d:2 respectively. The MnO_x phases identified by XRD analysis agree to that of observed HRTEM lattice fringes.

The chemical environment and oxidation states of as-deposited MnO_x films have been further probed using X-ray absorption near-edge structure spectroscopy (XANES) and X-ray photoelectron spectroscopy (XPS). The phases identified through diffraction techniques perfectly match to what observed by spectroscopic techniques. Valence states of Mn in the mixed-valence layer and tunnel structure manganese oxides (MnO_x), usually referred as phyllomanganates and

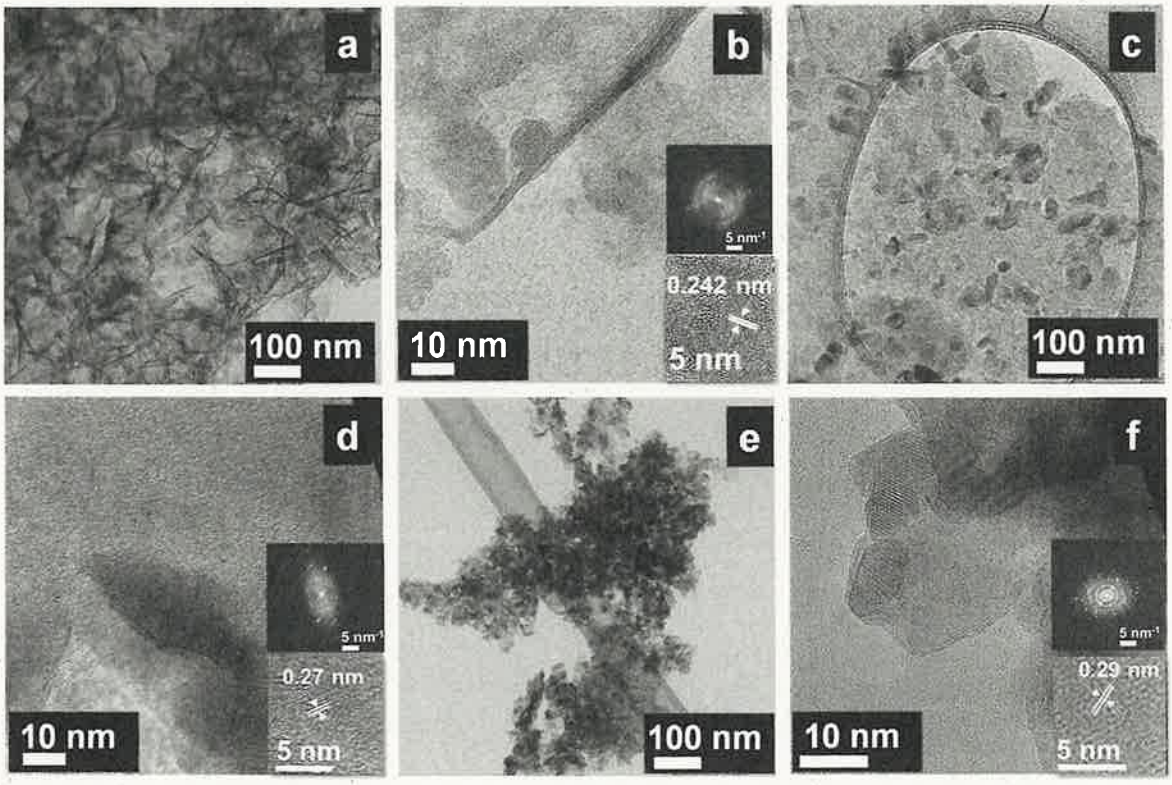

Fig. 2. HRTEM analysis of various deposited MnOx films; **(a, b)** 300 °C air, **(c, d)** 400 °C air, **(e, f)** 400 °C argon.

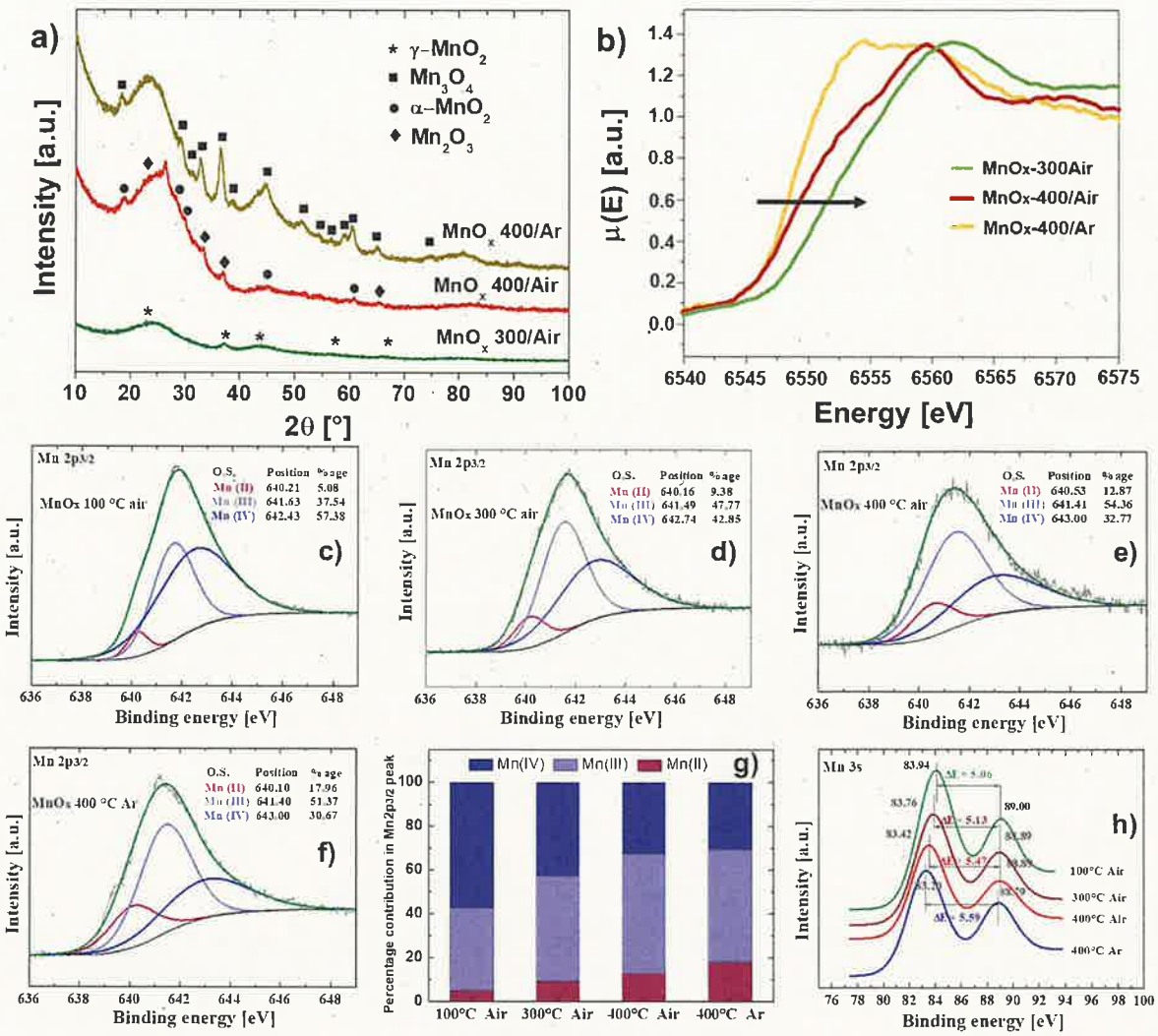

Fig. 3. (a) XRD diffraction patterns of various as-deposited MnO_x films; (b) Mn K edge XANES spectra for Mn as-prepared samples, energy edge position change with increasing valence value. XPS spectra Mn $2p^{3/2}$ of MnO_x samples that had different thermal treatments (c) MnO_x-100 °C/air, (d) MnO_x-300 °C/air, (e) MnO_x-400 °C/air and (f) MnO_x-400 °C/Ar. (g) percentage contributions of different oxidation states of Mn $2p^{3/2}$ for as-prepared samples. (h) Energy gaps between Mn3s peaks for estimation of oxidation states of as-prepared MnO_x samples.

tectomanganates, can be estimated by X-ray absorption near-edge structure (XANES) spectroscopy using Mn oxide standards with known oxidation states and performing a calibration curve between the valence band and, for example, edge energy shift. Fig. S4a shows the measured Mn K edge XANES spectra for the reference compounds (Mn, MnO, MnO_2, Mn_2O_3), and here energy edge position change indicated by the black arrow is in direct relationship with increasing valence state. While Fig. 3b reports Mn K edge XANES spectra for the MnO_x-300 °C/air, MnO_x-400 °C/air, and MnO_x-400 °C/Ar. In the present scenario, a method described by Manceau et al. is used to estimate the valence state of three MnO_x samples (Fig. 8) [43,48]. The valance states for the three MnO_x samples treated at 300 °C in air, 400 °C in air and argon is estimated as 2.9, 2.1, and 1.24 respectively.

XPS survey of the four samples namely MnO_x-100 °C/air, MnO_x-300 °C/air, MnO_x-400 °C/air and MnO_x-400 °C/Ar has been performed to determine the oxidation states at the surfaces of as prepared samples. The survey spectra of the samples showed Mn, O, C as the major surface elements. For valence state analysis, the spectra of Mn2p (633 eV–662 eV) and O1s (538 eV–523 eV) were measured. Additionally, the Mn3s signal (94 eV–76 eV) was measured. Deconvolutions were carried out to identify and quantify the species. Fig. 3c–f shows the XPS spectra corresponding to $Mn2p_{3/2}$ with the deconvolutions corresponding to each species of Mn. In all cases, the binding energy values for each component are consistent by the ranges reported in the literature [44,49]. The relative percentages of each Mn species present, calculated according to the relative areas of each peak, are listed in Table S1. Comparing the samples treated in air, it is observed that by increasing the temperature of the treatment, the percentage of Mn (II) increases and the percentage of Mn (IV) decreases. Regarding the sample that during the heat treatment was kept under Ar atmosphere, a higher percentage of Mn (IV) is observed at surface compared with the sample subjected to the same temperature but in the air. Fig. S4b shows the full width half mean (FWMH) values for deconvoluted Mn $3p_{3/2}$ spectra measured for the MnO_x samples that received different thermal treatments in air. Here, the width values are reported at the average height of the different components (FWHM). It is observed that as the temperature of the heat treatment increases, the widths of the peaks progressively increase [43,44].

Additionally, the corresponding Mn3s orbital signal was analyzed since it is also useful to estimate the oxidation state of Mn. The separation between the peaks corresponding to internal electrons originates due to the interaction of them with unpaired electrons of the valence band. This process takes place after irradiating the sample and "plucking" electrons from it. The separation ΔE between the peaks Mn3s will be

proportional to two factors: 1) the energy of the electronic interaction mentioned, 2) the total spin given by the unpaired electrons in levels 3s and 3d. Taking point 2, into account, the greater the oxidation state of Mn, the greater the total spin and the smaller the ΔE separation between the Mn3s two peaks. The measured ΔE results are shown in Table S1. It is observed that the values of ΔE measured for the samples take intermediate values between those measured for the patterns of Mn (II) and Mn (IV) ($MnCO_3$ and MnO_2 respectively) (Fig. 3h). For each sample, the average oxidation state for Mn was estimated according to previously published information [44,49]. For the quantitative description of oxygen vacancies on various MnO_x, the high resolution O1s XPS spectra of MnO_x300/Air and MnO_x400 in air and in argon have been analyzed. Each spectrum can be deconvoluted into two peaks that are assigned to lattice oxygen (around 530 eV) and non-lattice oxygen around 531 eV denoted at O_{ads}. Specifically, the existence of surface adsorbed oxygen species indicated the formation of oxygen vacancies. According to Zhang et al. [50], the ratio of the integrated areas under the non-lattice and the lattice oxygen peaks (O_{ads}/O_{latt}) represents relative oxygen vacancy concentration in MnO_x. As can be seen MnO_x 400/Air shows the lowest amount of surface-adsorbed oxygen owing to less abundant surface oxygen vacancies. In Fig. S5, MnO_x 300 in air and MnO_x 400 in argon show higher values of O_{ads}/O_{latt} implying a stronger interaction between the material and adsorbed oxygen species since the surface oxygen vacancies can be active centers in adsorbing the LiPS. MnO_x-400 Ar has a much higher proportion of O_{ads}, suggesting that it may have rich surface oxygen vacancies.

3.2. LiPS adsorption and electrocatalytic interaction through visual assessment test, XPS, and Li_2S precipitation test

To understand the interactions of these mixed states MnO_x on carbonized cellulosic fabric with LiPS, visual LiPS adsorption assessment experiments followed by detailed XPS analyses have been carried out. For the purpose, 5 mL of as prepared 25 mM Li_2S_6 solution is transferred

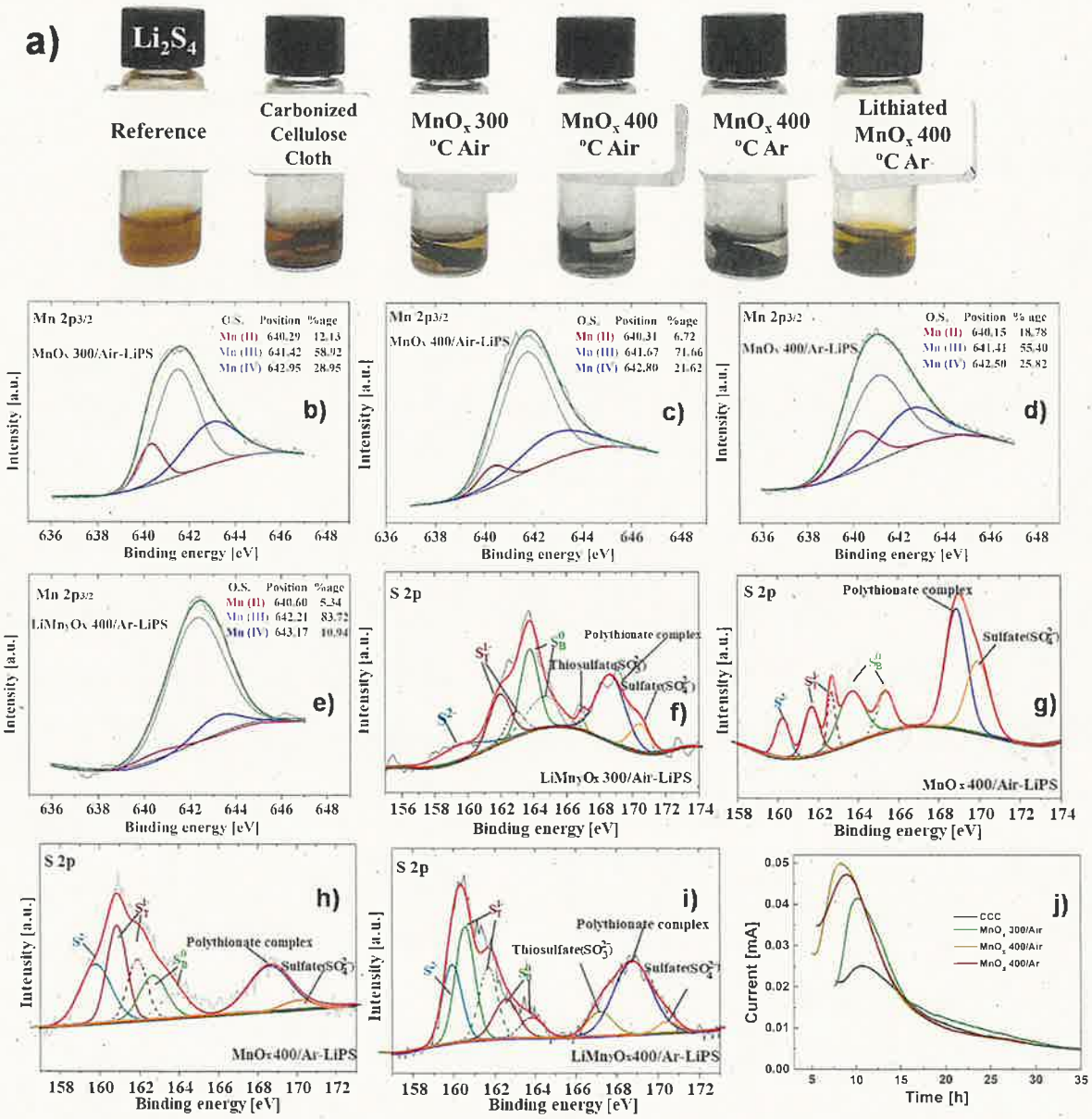

Fig. 4. (a) Experimental demonstration of LiPS adsorption capability of carbonized cellulose clothes deposited without/with MnO_x annealed at different conditions. XPS analysis of LiPS interacted MnO_x matrices; $Mn2p^{3/2}$ spectra for (b) MnO_x-300 °C/air, (c) MnO_x-400 °C/air, (d) MnO_x-400 Ar (e) $LiMn_yO_x$-400 °C/Ar. S2p spectra for (f) MnO_x-300 °C/air, (g) MnO_x-400 °C/air, (h) MnO_x-400 °C/Ar (i) $LiMn_yO_x$-400 °C/Ar. (j) Li_2S nucleation test of Li_2S_8/tetraglyme solution for carbonized cellulose clothes deposited without/with MnO_x annealed at different conditions.

into six glass vials, and 1 cm^2 of carbonized cellulose cloth with various depositions has been introduced into the vials. From the six vials, one was taken as control, second was introduced with bare carbonized cloth, third, fourth and fifth were introduced with MnO_x-300 °C/air, MnO_x-400 °C/air, and MnO_x-400 °C/Ar electrodeposited carbon clothes and sixth one was added with lithiated MnO_x-400 °C/Ar deposited carbon cloth. All samples' vials were shaken up well and left for 6 h to compare the change in color of LiPS solutions (Fig. 4a). It can be observed that there is no change in color against control for the vial introduced with bare carbonized cloth. While there is significant decolorization for the vials loaded with MnO_x electrodeposited carbon clothes. Decolorization for the three samples can be ranked as: MnO_x-400 °C/air, MnO_x-400 °C/Ar, MnO_x-300 °C/air (from high to low). Even for the sixth vial with lithiated MnO_x-400 °C/Ar, there is a drop in intensity with a shift in hue of the solution. To elucidate the interactions, detailed XPS analyses of Li_2S_6 interacted MnO_x electrodeposited carbonized electrodes were performed. For this, freestanding electrodes swatches had been recovered under stringent Argon atmosphere and transferred to XPS instrument. From the detailed XPS survey, the areas under $Mn2p_{3/2}$ and S2p high resolution peaks have been deconvoluted to observe the interactions and changes in chemical environment. Li_2S_6 solid demonstrates two S2p peaks at 161.8 and 163.2 eV corresponds to terminal (S_T^{-1}) and bridging (S_B^0) sulfur atoms respectively. But on encountering MnO_x, new oxidized sulfur peaks do appear at 167.2, 168.7 and 170.4 eV, which correspond to thiosulfate, polythionate complex and sulfate depending on the chemical configuration of MnO_x deposited films. The appearance of new peaks corroborates the fact that LiPS exhibit different redox reactions on interaction with different MnO_x phases. The oxidation of Li_2S_6 is on the expense of reduction of higher oxidation number MnO_x into lower ones as evident from the comparison of XPS spectra of pristine and Li_2S_6 absorbed MnO_x films. $Mn2p_{3/2}$ deconvoluted peaks appear around 642.7 eV (Mn^{4+}) exhibit a reduction in percentage area from 42.85, 32.77, and 30.67 for pristine to 28.95, 21.62, and 25.82 for Li_2S_6 interacted MnO_x-300 °C/air, MnO_x-400 °C/air, and MnO_x-400 °C/Ar respectively. This reduction in area corresponds to an increase in the areas for the peaks correspond to Mn^{3+} and Mn^{2+} phases. The most striking phenomenon is the shift in ratio of the peaks for LiPS and their oxidized form for various MnO_x phases. This ratio directly corresponds to the disappearance of color such as in case of MnO_x-400 °C/air, LiPS solution got completely transparent and the ratio of oxidized to LiPS sulfur's is the highest for the same. The strong oxidation of LiPS can even be visualized for the same sample from the intensity of sulfate (SO_4^{-2}) that is electrochemically irreversible product and does not participate in any sort of interaction in the battery. The narrow sulfate peak was observed for MnO_x-400 °C/Ar that confirms the heterostructure's optimality for better capacity retention and electrochemical performance. The least interaction is exhibited by MnO_x-300 °C/Air, the ratio of oxidized sulfur to LiPS sulfur one is the least correspondingly. Interestingly, even lithiated form of MnO_x-400 °C/Ar exhibited interactions with LiPS, and oxidized peak's deconvolution presents thiosulfate ($S_2O_3^{-2}$) that is important for polythionate complexes for LiPS retention. This portrays that MnO_x-400 °C/Ar even in lithiated form produces polythionate, referred as transfer mediator, could exhibit better electrochemical performance by restricting polysulfide at cathode surface. So, it can be inferred that MnO_x-400 °C/Ar substrate exhibits the right chemical interaction that is required to produce the species for reducing LiPS dissolution. These facts have been further corroborated by study of redox potentials of MnO_x hosts and will be discussed in subsequent section.

Li_2S precipitation reflects the suitability of the host matrix to augment the sulfur utilization and to improve the cycle life of the sulfur cathodes. In fact, Li_2S nucleation and growth test demonstrates the fast conversion of LiPS to Li_2S to restrict the LiPS shuttle and to accelerate the sluggish redox kinetics. Fig. 4j reports the Li_2S precipitation curves for bare CCC, MnO_x-300 °C/air, MnO_x-400 °C/air, and MnO_x-400 °C/Ar electrodeposited carbon clothes. The areas under the curves represents the capacities of Li_2S precipitation that can be estimated by current integration as per Faraday's Law. Bare carbonized cloth provides a smaller value for Li_2S precipitation than that of MnO_x deposited electrodes. MnO_x porous films annealed at 400 °C provided the highest and comparative value of Li_2S precipitation irrespective of treatment atmosphere. MnO_x annealed at 300 °C in air exhibited remarkable Li_2S nucleation but lower than that of MnO_x annealed at 400 °C. This suggests that MnO_x phases significantly improve the Li_2S nucleation capability of CCC but dependent on the oxidation states of MnO_x The intricate structure stays same for all types of MnO_x deposited on CCC hosts, but the strong change in Li_2S nucleation can only be referred to change of phases in MnO_x deposit.

3.3. Electrochemical response of MnO_x and MnO_x/S cathodes

Electrochemical responses of MnO_x-300 °C/air, MnO_x-400 °C/air, and MnO_x-400 °C/Ar electrodeposited carbon cloth self-standing electrodes have been probed through CV and EIS (Fig. 5a and b). From cyclic voltammetry, the redox potentials vs. Li/Li^+ of the three heterostructured MnO_x films annealed at 300 and 400 °C in air, and at 400 °C in Argon can be read as 3.04, 3.25 and 2.73 V respectively. MnO_x-400 °C/Ar film falls well in the voltage range ($2.4\ V \leq E^0 \leq 3.05\ V$ versus Li/Li^+) for the formation of thiosulfates that in turn assist polythionate complex formation [25]. On other hand, MnO_x-400 °C/air with the highest value of redox potential would cause overoxidation to sulfate ions that is electrochemically irreversible. These facts have already been witnessed in LiPS visual adsorption test and XPS of LiPS interacted MnO_x films. Areas under the redox peaks are relatively smaller for MnO_x-400 °C/Ar than that of MnO_x-300 °C/air, and MnO_x-400 °C/air, this represents relatively weak Faradic reactions. This also contributes towards the stability of the structures. However, the second reduction peak for MnO_x-400 °C/Ar can be detected around 1.7 V that does appear within Li/S cell cut-off potential for charging and discharging. This peak could irreversibly contribute towards the lithiation and stability of post-spinel structures. EIS of these electrodes have depicted the typical response of supercapacitive materials (Fig. 5b). CV for sulfur loaded MnO_x/S 300 °C air, MnO_x/S 400 °C air, MnO_x/S 400 °C Ar cathodes have been performed (Fig. 5c–e). CV profiles for all three electrodes were broadened because of higher sulfur loading, but the sulfur reduction and oxidation peaks can be observed well in the theoretical range of sulfur Faradic peaks. Reduction is in the potential range of 2.4 to 2.0 V and oxidation is in the range of 2.4–2.6 V. In addition to these principal redox peaks, small redox peaks can be traced out that are linked to the lithiation and delithiation of MnO_x films as observed in pristine electrodes (indicated by arrows). This lithiation followed by partial delithiantion could greatly impact the stability of MnO_x porous films. In some cases, this partial lithiation/delithiation could disrupt the crystal structure integrity and cause the disruption of MnO_x film [51,52]. However, in other cases, it can develop a stable crystalline structure that limit the dissociation of porous oxide film [53]. Later can be observed in case of MnO_x/S 400 °C Ar, where Mn_3O_4 spinel transform into stable post-spinel structure.

To validate these observations, detailed EDS analyses have been performed of the exhausted polypropylene separators subjected to five cycles of CV. Figs. S6a, b, c presents EDS analyses of the surfaces of exhausted polypropylene separator recovered from Li/S cells comprised of MnO_x/S 300 °C air, MnO_x/S 400 °C air, and MnO_x/S 400 °C Ar based sulfur cathodes respectively. It can be observed that there is no trace of Mn on the separator recovered from cell comprised of sulfur loaded MnO_x/S 400 °C Ar cathode. For further confirmation, SEM and elemental mapping (Fig. S7) have been carried out of the separator surfaces. The morphology and nature of deposits on the PP separator can assist to better understand the transitions that were going on during electrochemical processes. This will be discussed in detail in later section, but presence of Mn in elemental map of MnO_x/S 300 °C air, and MnO_x/S 400 °C air, and absence of the same in elemental map of MnO_x/

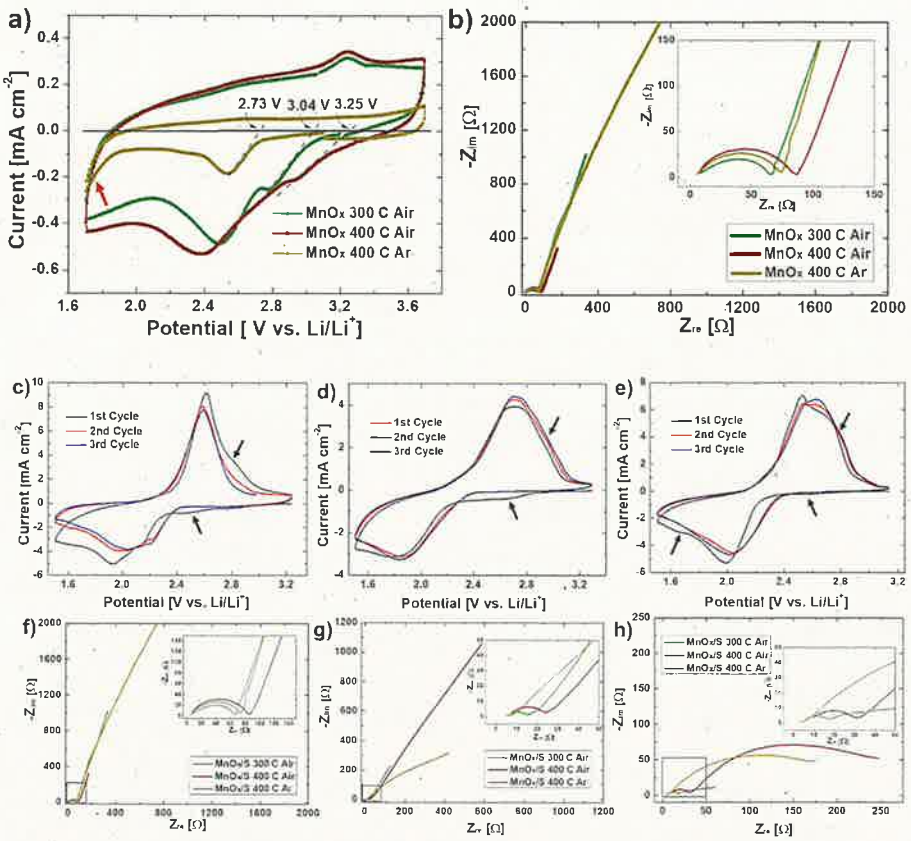

Fig. 5. (a) Cyclic voltammetry of various MnO_x phases electrodeposited on carbonized cotton cloth demonstrating their corresponding redox potential. Redox potential value for each structure is evaluated from slope intersect of first reduction peak; (b) EIS of various MnO_x phases electrodeposited on carbonized cotton cloth; Cyclic voltammetry of free-standing (c) MnO_x/S 300 °C Air, (d) MnO_x/S 400 °C Air, (e) MnO_x/S 400 °C Ar sulfur cathodes signifying the redox contributions from MnO_x phases; EIS of various MnO_x/S cathodes at (f) open circuit potential, after (g) first cycle of CV (h) five cycles of CV.

S 400 °C Ar points out the stability of the MnO_x film crystalline structure. EIS measurements for all three MnO_x/S cathodes were carried out at open circuit potential of assembled cell, after first cycle of CV and after five cycles of CV. It can be observed from Fig. 5 f-h and insets that there is an initial drop in charge transfer resistance (R_{ct}) values, diameters of the semicircle at high frequencies, of MnO_x/S cathodes. Small R_{ct} value signifies high conductivity and strong affinity of MnO_x matrices towards LiPS. There is slight increase in R_{ct} values due to deposition of sulfur products into porous cathode architecture. This phenomenon can be observed by post-mortem analysis of cathodes in subsequent section. At low frequencies, all the cells exhibited the Warburg impedance at open circuit potential, but with cycling there is appearance of second large semicircle for the 300 °C/Air and 400 °C/Ar cathodes. This exhibits the appearance of the second time constant for the representative electrochemical systems. This phenomenon could be referred to as mass transport resistance that is due to cathode material activation. The lower time constant value in MnOx/S 400 °C/Ar represents better electrochemical performance, that is also evident in GCD.

Galvanostatic charging and discharging have been carried out for all as-prepared freestanding MnO_x/S 300 °C air, MnO_x/S 400 °C air, MnO_x/S 400 °C Ar and bare CCC sulfur cathodes. The sulfur loading for MnO_x/S cathodes was kept around 5 mg cm^{-2} and for bare CCC/S cathode 2.4 mg cm^{-2} unless mentioned. Fig. 6a reports cyclic performances of Li/S cells built from MnO_x/S ,300 °C air, MnO_x/S 400 °C air, and MnO_x/S 400 °C Ar. The best performance exhibited by cell comprised of MnO_x/S 400 °C Ar sulfur cathode followed by MnO_x/S 300 °C air, and MnO_x/S 400 °C air respectively. For the very first cycle, MnO_x/S 400 °C Ar sulfur cathode exhibited the discharge capacity of 1153.7 mA h g^{-1} at C/10 (1 C = 1672 mA/g), while for second cycle at C/5 the discharge capacity of 824 mA h g^{-1} has been recorded that rises to 876.4 mA h g^{-1}. There is literally no loss in capacity for this cathode for next 150 cycles. MnO_x/S 300 °C air sulfur cathode demonstrated an initial capacity of 1085.9 mA h g^{-1} at C/10 for first cycle, 770 mA h g^{-1} for second cycle at C/5 that reached to a maximum value of 830.7 mA h g^{-1} with capacity loss of 0.04% per cycle for 150 cycles. MnO_x/S 400 °C air sulfur cathode showed an initial capacity of 1077.5 mA h g^{-1} for first cycle at C/10, 685.67 mA h g^{-1} for second cycle at C/5 that reached to a maximum value of 688.7 mA h g^{-1} with capacity loss of 0.09% per cycle for 150 cycles. The initial rise in capacity for these self-standing high loading cathodes could be owing to incomplete soaking of cathode with electrolyte and inadequate activation of high loading active material initially. Nevertheless, it can be observed that the best performance revealed by MnO_x/S 400 °C Ar sulfur cathode due to presence of oxygen deficient phases with right heterostructure to accommodate the electrochemical changes in the host. When MnO_x/S 400 °C Ar cathode with sulfur loading of 2.4 mg cm^{-2} was cycled against CCC/S cathode, it can be observed that initial discharge capacity is 1206 mA h g^{-1} for the former and 919.4 mA h g^{-1} for later at C/10. After cycling for 150 cycles, MnO_x/S 400 °C Ar cathode specific capacity retained at 943.68 mA h g^{-1} while for CCC/S cathode it dropped to 318 mA h g^{-1} at C/5 (Fig. 6 b-d). The potential gap (ΔE) between lower discharge and upper charge plateaus for MnO_x/S 400 °C Ar cathode is minimal and stay constant after long-term cycling, while for CCC/S it is widened by every next cycle probably due to extreme shuttling of LiPS and deposition of Li_2S on electrode surface. This confirms that MnO_x deficient phases pose a reduced polarization and facilitate reaction kinetics. These results are exactly in line with what was observed during adsorption test, XPS and CV analysis of these host materials.

To further underline the ongoing mechanisms and understand the varying electrochemical performances, detailed post-mortem analyses of exhausted cathodes have been performed and will be discussed in next section. The average Coulombic efficiency was estimated and found 98%, 96%, 93.5% and 95.5% for MnO_x/S 400 °C Ar, MnO_x/S 300 °C air, MnO_x/S 400 °C air and CCC/S based cathodes respectively. The rate capabilities of MnO_x/S 400 °C Ar and CCC/S cathodes were evaluated by increasing the current densities from 0.1 to 2 C for every 5 cycles and

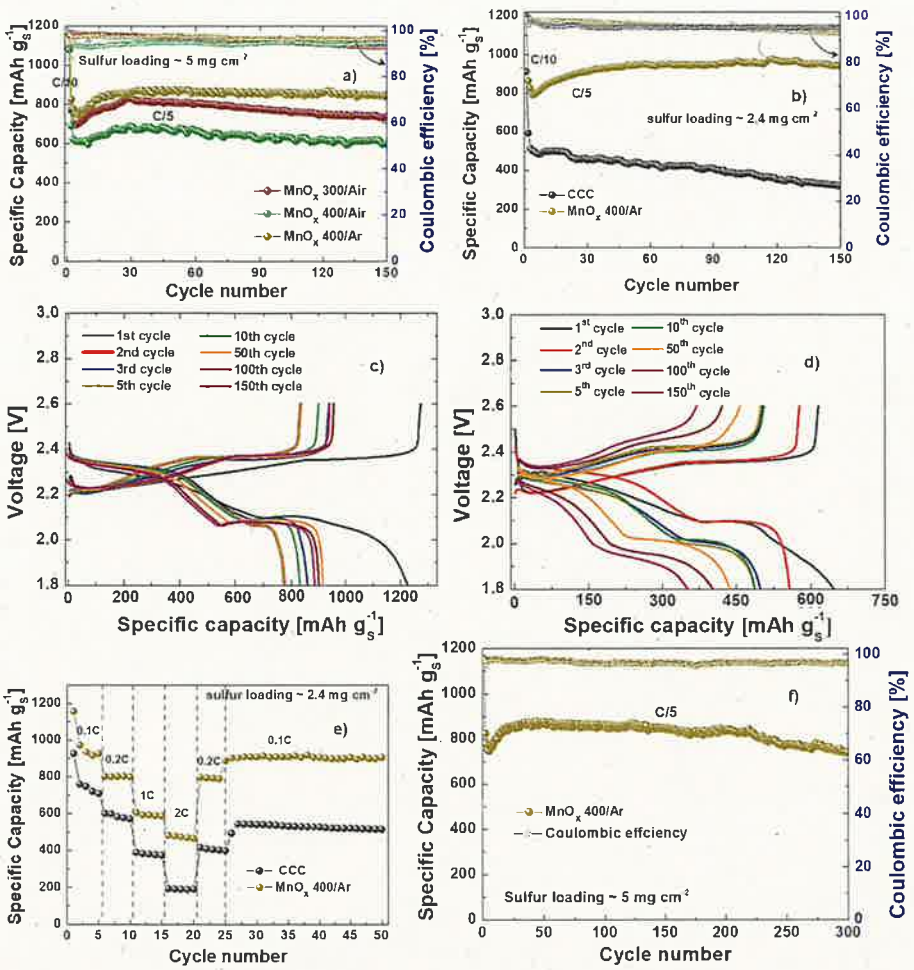

Fig. 6. (a) Long-term Galvanostatic charge-discharge cycling performance of freestanding MnO_x deposited carbonized cellulose cloth as a cathode at 5 mg sulfur loading. (b) cyclic performance comparison of MnO_x/S 400 °C Ar cathode at 5 mg loading vs. CCC/S cathode at 2.4 mg loading. Charge and discharge profiles of (c) MnO_x/S 400 °C Ar cathode at 5 mg loading freestanding and (d) CCC/S cathode at 2.4 mg loading. (e) C-rate performances of MnO_x/S 400 °C Ar cathode and CCC/S cathode at 2.4 mg loading. (f) long-term capacity retention of free-standing MnO_x/S 400 °C Ar cathode at 5 mg loading.

back to 0.1 C for further cycling. The MnO_x/S 400 °C Ar cathode realizes reversible discharge capacity of 1107.6, 812.86, 641.24, 518.54 mA h g^{-1} at 0.1, 0.2, 1 and 2C respectively. On getting back to 0.2 and 0.1 C, the discharge capacities of 773.8 and 901.24 mA h g^{-1} have been observed. While CCC/S cathode has exhibited much lower discharge capacities. MnO_x/S 400 °C Ar cathode has been cycled for 300 cycles at loading of 5 mg cm^{-2} at 0.2 C with capacity decay of only 0.03% per cycle.

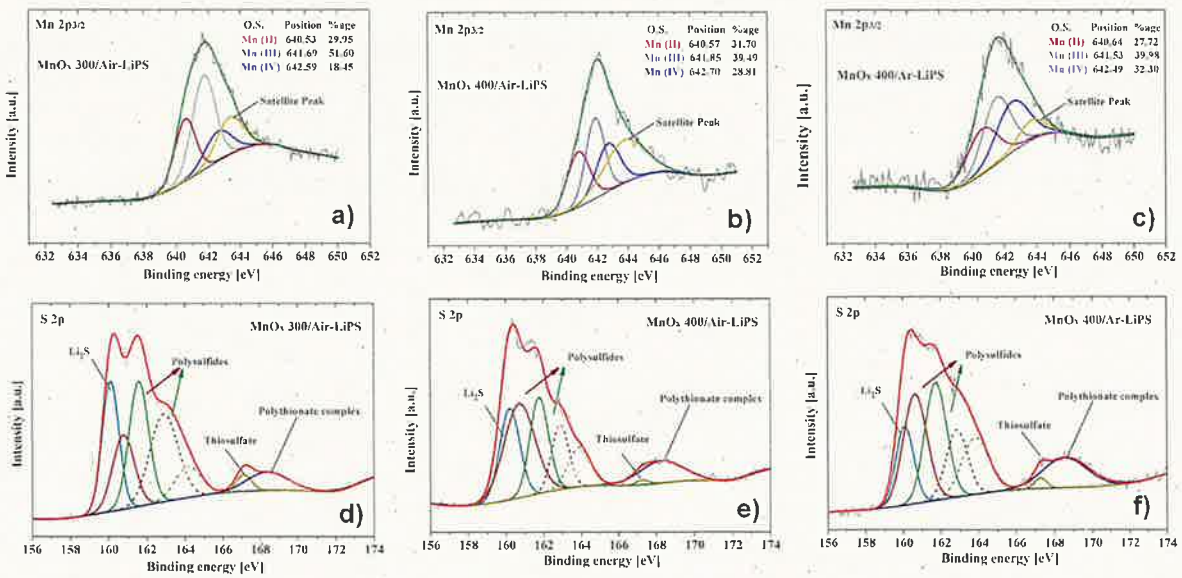

Fig. 7. XPS analyses of exhausted sulfur cathodes; $Mn2p^{3/2}$ spectra for (a) MnO_x/S 300 °C air cathode, (b) MnO_x/S 400 °C air cathode, and (c) MnO_x/S 400 °C Ar cathode. S2p spectra for (a) MnO_x/S 300 °C air cathode, (b) MnO_x/S 400 °C air cathode, and (c) MnO_x/S 400 °C Ar cathode.

3.4. Post-mortem analyses of exhausted cells

To investigate the change in chemical environment of exhausted electrode, detailed XPS and XANES analysis have been performed for 150 cycles drained electrodes. Additionally, SEM and EDX analyses for PP separators recovered from CV has been carried out. Fig. 7 demonstrates the deconvolution of $Mn2p_{3/2}$ and S2p high resolution peaks. It can be observed that all three electrodes came up with a satellite peak in addition to Mn (II, III and IV) peaks. The exact position of satellite peak is not properly stated in literature but peaks beyond 644 eV are mostly stated as satellite [54]. In current work, the region beyond the designated peak positions is assigned for satellite feature and is only appeared in exhausted cathodes. This satellite peaks could arise due to deposition of Li_2S and other products interacting with MnO_x phases. There is an observable reduction in area for the Mn^{4+} peaks for MnO_x/S 300 °C air and MnO_x/S 400 °C air cathodes, in contrast to MnO_x/S 400 °C Ar cathode. This observation points out towards the stability of heterostructure attained in MnO_x/S 400 °C Ar cathode. Observation of S2p peaks for all three cathodes reveals some interesting chemical events that happened during cycling. Li_2S can be observed for all three cathodes that was not discernible in previous investigation with LiPS. This points out the deposition of Li_2S onto the surface of electrodes. However, the intensity of Li_2S against LiPS peaks is varying significantly in all three cases. The least intensity for this peak can be observed for MnO_x/S 400 °C Ar cathode. Similarly, oxidation peak for sulfur, represents polythionate complex formation, exhibited greater intensity for MnO_x/S 400 °C Ar cathode in contrast to other two cathodes. For MnO_x/S 400 °C air cathode, thiosulfate peak is insignificant.

These all observations from exhausted cathodes are corroborating the inferences deduced from XPS analyses for MnO_x/LiPS interacted substrates. XANES analyses of Mn K edge for all three exhausted electrodes bring out that there is change in valance state of all three heterostructures (Fig. 8 c-e). There is a decline in valance state for MnO_x/S 300 °C air and MnO_x/S 400 °C air cathodes, whilst oxidation state for MnO_x/S 400 °C Ar cathode shift to higher state. This again could be explained in the light of CV curve, where incomplete delithiation for MnO_x 400 °C/Ar cathode left the structure in higher oxidation state and inculcate the stability towards heterostructure. SEM/EDS analyses of PP separator further strengthen this claim. There is no leaching out of Mn from MnO_x/S 400 °C Ar cathode, though for other two cathodes Mn can be detected onto surface of separator through EDS. For separators recovered from Li/S cells built of MnO_x/S 300 °C air and MnO_x/S 400 °C air cathodes, large deposits can be detected of species made of sulfur. On the other hand, for separator recovered from MnO_x/S 400 °C Ar cathode, small islands of sulfur deposit can be observed (Fig. S6). This largely points out the capability of cathode to limit LiPS dissolution and their shuttling to other side. The most interestingly the separator recovered from MnO_x/S 400 °C Ar cell demonstrated no signs of Mn both in EDX and elemental mapping analyses. This confirms that MnO_x 400 °C/Ar exhibited the most stable heterostructure that not only proves efficient in restraining LiPS shuttle by interacting with them but also enables to realize high-loading freestanding and long-life sulfur cathodes.

4. Conclusions

In summary, authors have successfully architecture the freestanding host cathodes constituted of electrodeposited MnO_x nanoflakes on carbonized cellulose clothes for higher sulfur loadings and low electrolyte content. MnO_x nanoflakes have been surface engineered by controlling the annealing conditions to realize different oxidation states to underline the polysulfide interaction at defected sites for better electrochemical performances. From adsorption test, XPS, and XANES analyses, it can be observed that defected interfaces enhance the reaction activity and promote polythionate formation for retention of LiPS on cathode surface. Additionally, lower oxidation state MnO_x films exhibited optimal redox potential for conversion of sulfides into thiosulfates for complexation and better structural stability for long cycling performance. The cathodes bearing high oxygen-deficient manganese oxide nanoflakes achieve high initial discharge capacity of 1153.7 mA h g^{-1} at 0.1 C and high reversible capacity of 824 mA h g^{-1} at 0.5 C over 200 cycles at sulfur areal loading of 5 mg cm^{-2}, while only initial discharge capacity of 1085.9 mA h g^{-1} and reversible capacity of 410 mA h g^{-1} are obtained for MnO_2 rich heterostructure film. This study proposes that freestanding sulfur cathodes with surface engineered

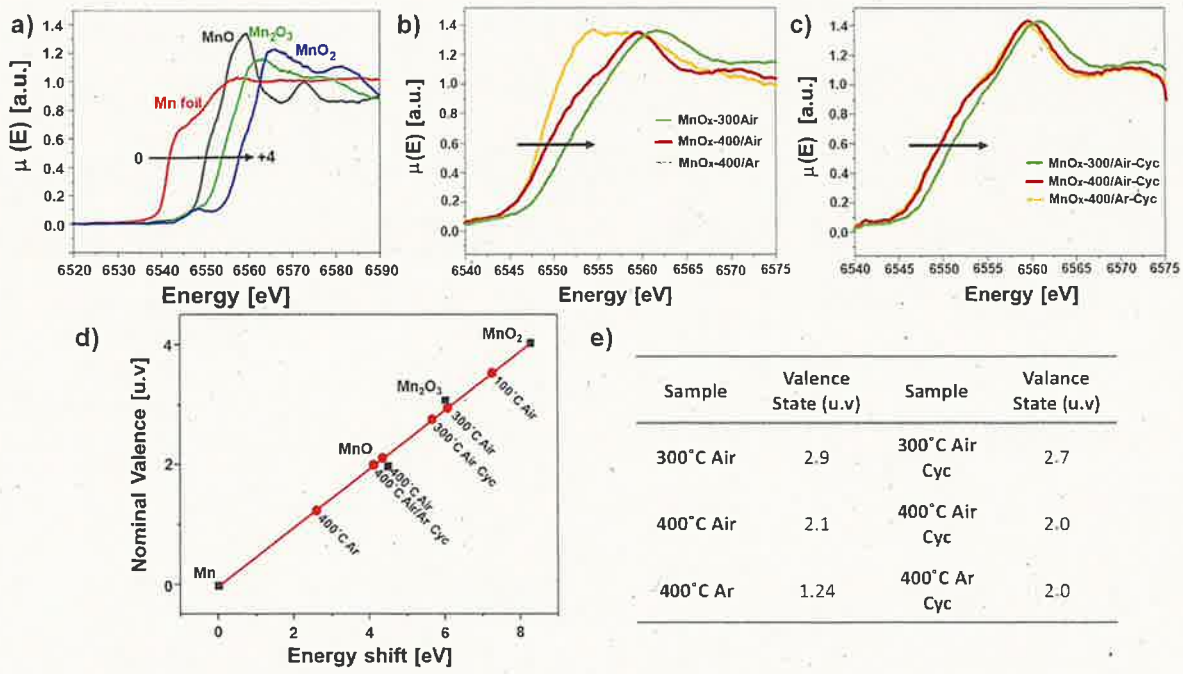

Sample	Valence State (u.v)	Sample	Valance State (u.v)
300°C Air	2.9	300°C Air Cyc	2.7
400°C Air	2.1	400°C Air Cyc	2.0
400°C Ar	1.24	400°C Ar Cyc	2.0

Fig. 8. (a) Mn K edge XANES spectra for Mn reference compounds, energy edge position change with increasing valence value. b) Mn K edge XANES spectra for as-developed samples. c) Mn K edge XANES spectra for exhausted electrodes. d) Plot of nominal valence states of Mn vs. energy shifts from XENAS. e) Table depicting the valence states of Mn for as-prepared samples and exhausted electrodes.

highly porous MnO_x films on cellulosic carbon cloth can be effectively fabricated to enhance the conversion and mediation of LiPS. This retention of LiPS at cathode could be attributed to physical entrapment by highly porous cellulosic carbon cloth and chemically by promoting the formation of insoluble surface bound intermediates. The strategy could be extended to other metal oxides cathodes by architecting and surface engineering of deposited films.

CRediT authorship contribution statement

Usman Zubair: Conceptualization, Methodology, Writing – original draft. **Khalil Jori:** Formal analysis. **Jorge E. Thomas:** Investigation, Data curation. **Julia Amici:** Visualization, Formal analysis. **Carlotta Francia:** Project administration, Resources, Writing – review & editing. **Silvia Bodoardo:** Supervision, Funding acquisition.

Declaration of competing interest

The authors declare that they have no known competing financial interests or personal relationships that could have appeared to influence the work reported in this paper.

Data availability

Data will be made available on request.

Acknowledgments

Financial support was provided by the European Union H2020 NMP-17-2014 ALISE (GA 666157), This work was partially funded by CONICET, Agencia Nacional de Promoción Científica y Tecnológica (PICT 2019-0784), Universidad Nacional de La Plata and Laboratorio Nacional de Luz Sincrotron (proposal DXAS 20170908).

Appendix A. Supplementary data

Supplementary data to this article can be found online at https://doi.org/10.1016/j.jpowsour.2023.233457.

References

[1] S.-H. Chung, C.-H. Chang, A. Manthiram, Progress on the Critical Parameters for Lithium–Sulfur Batteries to Be Practically Viable, 28, 2018, 1801188, 28.
[2] Y.-T. Liu, S. Liu, G.-R. Li, X.-P. Gao, Strategy of Enhancing the Volumetric Energy Density for Lithium–Sulfur Batteries, 33, 2021, 2003955, 8.
[3] A. Bhargav, J. He, A. Gupta, A. Manthiram, Lithium-sulfur batteries: attaining the critical metrics, Joule 4 (2) (2020) 285–291, 2020/02/19.
[4] P. Wang, B. Xi, M. Huang, W. Chen, J. Feng, S. Xiong, Emerging Catalysts to Promote Kinetics of Lithium–Sulfur Batteries, 11, 2021, 2002893, 7.
[5] X. Ji, L.F. Nazar, Advances in Li–S batteries, J. Mater. Chem. 20 (44) (2010) 9821–9826, 10.1039/B925751A.
[6] Y. Xiao, et al., Operando soft X-ray absorption spectroscopic study on microporous carbon-supported sulfur cathodes, RSC Adv. 10 (65) (2020) 39875–39880, 10.1039/D0RA08299F.
[7] U. Zubair, J. Amici, S.M. Crespiera, C. Francia, S. Bodoardo, Rational design of porous carbon matrices to enable efficient lithiated silicon sulfur full cell, Carbon 145 (2019) 100–111, 2019/04/01.
[8] F. Liu, et al., Graphene foam current collector for high-areal-capacity lithium–sulfur batteries, ACS Appl. Nano Mater. 4 (1) (2021) 53–60, 2021/01/22.
[9] Z. Wu, et al., Phosphorous/oxygen co-doped mesoporous carbon bowls as sulfur host for high performance lithium-sulfur batteries, J. Power Sources 450 (2020), 227658, 2020/02/29.
[10] U. Zubair, D. Versaci, M. Umer, J. Amici, C. Francia, S. Bodoardo, Lithium polysulfides immobilization exploiting formate-ion doped polyaniline wrapped carbon for Long cycle life sulfur cathodes via conventional electrode processing, Mater. Today Commun. 26 (2021), 101970, 2021/03/01.
[11] W. Wang, et al., Defect-rich multishelled Fe-doped Co3O4 hollow microspheres with multiple spatial confinements to facilitate catalytic conversion of polysulfides for high-performance Li–S batteries, ACS Appl. Mater. Interfaces 12 (11) (2020) 12763–12773, 2020/03/18.
[12] Y. Song, et al., Vanadium dioxide-graphene composite with ultrafast anchoring behavior of polysulfides for lithium-sulfur batteries, ACS Appl. Mater. Interfaces 10 (18) (2018) 15733–15741.
[13] Y. Tao, et al., Kinetically-enhanced polysulfide redox reactions by Nb2O5 nanocrystals for high-rate lithium-sulfur battery, Energy Environ. Sci. 9 (10) (2016) 3230–3239, https://doi.org/10.1039/C6EE01662F.
[14] N. Li, et al., High-rate lithium-sulfur batteries enabled via vanadium nitride nanoparticle/3D porous graphene through regulating the polysulfides transformation, Chem. Eng. J. 398 (2020/10/15/2020), 125432.
[15] B. Hao, et al., Reviving catalytic activity of nitrides by the doping of the inert surface layer to promote polysulfide conversion in lithium-sulfur batteries, Nano Energy 60 (2019) 305–311, 2019/06/01.
[16] C.Y. Zhang, et al., Deciphering the catalysis essence of vanadium self-intercalated two-dimensional vanadium sulfides (V5S8) on lithium polysulfide towards high-rate and ultra-stable Li-S batteries, Energy Storage Mater. 43 (2021) 471–481, 2021/12/01.
[17] F. Zhou, et al., Low cost metal carbide nanocrystals as binding and electrocatalytic sites for high performance Li-S batteries, Nano Lett. 18 (2) (Feb 14 2018) 1035–1043.
[18] X. Liang, Y. Rangom, C.Y. Kwok, Q. Pang, L.F. Nazar, Interwoven MXene Nanosheet/Carbon-Nanotube Composites as Li–S Cathode Hosts, vol. 29, 2017, 1603040, 3.
[19] K. Xiao, et al., N-doped carbon sheets arrays embedded with CoP nanoparticles as high-performance cathode for Li-S batteries via triple synergistic effects, J. Power Sources 455 (2020), 227959, 2020/04/15.
[20] M. Zhao, et al., Electrochemical Phase Evolution of Metal-Based Pre-catalysts for High-Rate Polysulfide Conversion, vol. 59, 2020, pp. 9011–9017, 23.
[21] J. He, A. Bhargav, A. Manthiram, Molybdenum Boride as an Efficient Catalyst for Polysulfide Redox to Enable High-Energy-Density Lithium–Sulfur Batteries, vol. 32, 2020, 2004741, 40.
[22] W. Sun, Y. Li, S. Liu, C. Liu, X. Tan, K. Xie, Mechanism investigation of iron selenide as polysulfide mediator for long-life lithium-sulfur batteries, Chem. Eng. J. 416 (2021), 129166, 2021/07/15.
[23] M. Rana, et al., Oriented nanoporous MOFs to mitigate polysulfides migration in lithium-sulfur batteries, Nano Energy 75 (2020), 105009, 2020/09/01.
[24] U. Zubair, S. Bianco, J. Amici, C. Francia, S. Bodoardo, Probing the interaction mechanism of heterostructured VOxNy nanoparticles supported in nitrogen-doped reduced graphene oxide aerogel as an efficient polysulfide electrocatalyst for stable sulfur cathodes, J. Power Sources 461 (2020), 228144, 2020/06/15.
[25] X. Liang, C. Hart, Q. Pang, A. Garsuch, T. Weiss, L.F. Nazar, A highly efficient polysulfide mediator for lithium-sulfur batteries, Nat. Commun. 6 (2015) 5682.
[26] D. Rao, S. Yang, X. Yan, Surface atomic configurations of MnO2 regulating the immobilization of sulfides in lithium sulfur battery, J. Phys. Chem. C 124 (10) (2020) 5565–5573, 2020/03/12.
[27] B. Pandit, et al., High stability and long cycle life of rechargeable sodium ion battery using manganese oxide cathode: a combined density functional theory (DFT) and experimental study, ACS Appl. Mater. Interfaces 13 (9) (2021) 11433–11441, 2021/03/10.
[28] J. Li, et al., Mn3(PO4)2/rGO as dual-function polysulfide inhibitor through oxygen deficiencies and polar sites for lithium sulfur batteries, Appl. Surf. Sci. 521 (2020), 146425, 2020/08/15.
[29] G. Huo, et al., γ-MnO2 nanorod-assembled hierarchical micro-spheres with oxygen vacancies to enhance electrocatalytic performance toward the oxygen reduction reaction for aluminum-air batteries, J. Energy Chem. 51 (2020), 04/01.
[30] E. Saputra, S. Muhammad, H. Sun, H.-M. Ang, M.O. Tadé, S. Wang, Manganese oxides at different oxidation states for heterogeneous activation of peroxymonosulfate for phenol degradation in aqueous solutions, Appl. Catal. B Environ. 142–143 (2013) 729–735, 2013/10/01.
[31] A. Rafique, et al., Binder Free and Flexible Asymmetric Supercapacitor Exploiting Mn3O4 and MoS2 Nanoflakes on Carbon Fibers, vol. 10, 2020, p. 1084, 6.
[32] X. Chen, et al., Free-standing Mn3O4@CNF/S paper cathodes with high sulfur loading for lithium–sulfur batteries, ACS Appl. Mater. Interfaces 10 (16) (2018) 13406–13412, 2018/04/25.
[33] J. Guo, X. Zhang, X. Du, F. Zhang, A Mn3O4 nano-wall array based binder-free cathode for high performance lithium–sulfur batteries, J. Mater. Chem. 5 (14) (2017) 6447–6454, 10.1039/C7TA00475C.
[34] J. Wu, Q. Ma, C. Lian, Y. Yuan, D. Long, Promoting polythionate intermediates formation by oxygen-deficient manganese oxide hollow nanospheres for high performance lithium-sulfur batteries, Chem. Eng. J. 370 (2019).
[35] G. Radhika, P. Rajkumar, R. Subadevi, M. Sivakumar, Manganese and Graphene Oxide Composite as Highly Effective Sulfur Host for Enlightening Electrochemical Kinetics of Lithium-Sulfur Batteries, vol. 45, 2021, pp. 5214–5223, 4.
[36] B. Zheng, N. Li, J. Yang, J. Xi, Waste cotton cloth derived carbon microtube textile: a robust and scalable interlayer for lithium–sulfur batteries, Chem. Commun. 55 (16) (2019) 2289–2292, 10.1039/C8CC09973A.
[37] B. Babakhani, D.G. Ivey, Effect of electrodeposition conditions on the electrochemical capacitive behavior of synthesized manganese oxide electrodes, J. Power Sources 196 (24) (2011) 10762–10774, 2011/12/15.
[38] Y.-C. Chen, et al., Highly flexible supercapacitors with manganese oxide nanosheet/carbon cloth electrode, Electrochim. Acta 56 (20) (2011) 7124–7130, 2011/08/01/.
[39] S. Chou, F. Cheng, J. Chen, Electrodeposition synthesis and electrochemical properties of nanostructured γ-MnO2 films, J. Power Sources 162 (1) (2006) 727–734, 2006/11/08.
[40] A. Ramírez, P. Hillebrand, D. Stellmach, M.M. May, P. Bogdanoff, S. Fiechter, Evaluation of MnOx, Mn2O3, and Mn3O4 electrodeposited films for the oxygen evolution reaction of water, J. Phys. Chem. C 118 (26) (2014) 14073–14081, 2014/07/03.

[41] Z. Gao, Y. Zhang, N. Song, X. Li, Biomass-derived renewable carbon materials for electrochemical energy storage, Mater. Res. Lett. 5 (2) (2017) 69–88, 2017/03/04.
[42] S.-H. Chung, C.-H. Chang, A. Manthiram, A carbon-cotton cathode with ultrahigh-loading capability for statically and dynamically stable lithium–sulfur batteries, ACS Nano 10 (11) (2016) 10462–10470, 2016/11/22.
[43] Z. Geng, et al., δ-MnO2–Mn3O4 nanocomposite for photochemical water oxidation: active structure stabilized in the interface, ACS Appl. Mater. Interfaces 8 (41) (2016) 27825–27831, 2016/10/19.
[44] H.A. Le, S. Chin, E. Park, L.T. Linh, G.-N. Bae, J. Jurng, Chemical vapor synthesis and characterization of manganese oxides, Chem. Vap. Depos. 17 (7-9) (2011) 228–234.
[45] B. Zhang, et al., Crystallization design of MnO2via acid towards better oxygen reduction activity, CrystEngComm 18 (36) (2016) 6895–6902, https://doi.org/10.1039/C6CE01131D.
[46] W. Yang, J. Zhang, Q. Ma, Y. Zhao, Y. Liu, H. He, Heterogeneous reaction of SO2 on manganese oxides: the effect of crystal structure and relative humidity, Sci. Rep. 7 (1) (2017) 4550, 2017/07/03.
[47] G. Jian, Y. Xu, L.-C. Lai, C. Wang, M.R. Zachariah, Mn3O4 hollow spheres for lithium-ion batteries with high rate and capacity, J. Mater. Chem. 2 (13) (2014) 4627–4632, 10.1039/C4TA00207E.
[48] A. Mánceau, A. Marcus Matthew, S. Grangeon, Determination of Mn valence states in mixed-valent manganates by XANES spectroscopy, Am. Mineral. 97 (2012) 816.
[49] J.L. Junta, M.F. Hochella, Manganese (II) oxidation at mineral surfaces: a microscopic and spectroscopic study, Geochem. Cosmochim. Acta 58 (22) (1994) 4985–4999, 1994/11/01.
[50] L. Zhang, S. Wang, L. Lv, Y. Ding, D. Tian, S. Wang, Insights into the reactive and deactivation mechanisms of manganese oxides for ozone elimination: the roles of surface oxygen species, Langmuir 37 (4) (2021) 1410–1419, 2021/02/02.
[51] M.M. Thackeray, Manganese oxides for lithium batteries, Prog. Solid State Chem. 25 (1) (1997) 1–71, 1997/01/01.
[52] X. Hao, X. Lin, W. Lu, B.M. Bartlett, Oxygen vacancies lead to loss of domain order, particle fracture, and rapid capacity fade in lithium manganospinel (LiMn2O4) batteries, ACS Appl. Mater. Interfaces 6 (14) (2014) 10849–10857, 2014/07/23.
[53] H. Xia, Y.S. Meng, X. Li, G. Yuan, C. Cui, Porous manganese oxide generated from lithiation/delithiation with improved electrochemical oxidation for supercapacitors, J. Mater. Chem. 21 (39) (2011) 15521–15526, 10.1039/C1JM12767E.
[54] A. Ghods, C. Zhou, T.T. Ferguson, Structural and optical properties of (Zn,Mn)O thin films prepared by atomic layer deposition, J. Vac. Sci. Technol. A 38 (4) (2020).